Article

Methanation of CO_2 over High Surface Nickel/Aluminates Compounds Prepared by a Self-Generated Carbon Template

Sarra Roudane [1], Noureddin Bettahar [1], Alfonso Caballero [2] and Juan Pedro Holgado [2,*]

[1] Laboratoire de Chimie des Matériaux Inorganiques et Applications, Université des Sciences et de la Technologie d'Oran, Mohamed-Boudiaf, l Mnaouar BP 1505, Bir El Djir 31000, Oran, Algeria

[2] Departamento de Química Inorgánica, Instituto de Ciencia de Materiales de Sevilla (CSIC-US), Av. Américo Vespucio, 49, 41092 Sevilla, Spain

[*] Correspondence: jp.holgado@csic.es

Abstract: Catalytic gas-phase hydrogenation of CO_2 into CH_4 was tested under three different nickel/aluminate catalysts obtained from precursors of hexaaluminate composition ($MAl_{16}O_{19}$, M = Mg, Ca, Ba). These catalysts were prepared using a carbon template method, where carbon is self-generated from a sol-gel that contains an excess of citric acid and the Al and M salts (Ba^{2+}, Ca^{2+}, Mg^{2+}) by two-step calcination in an inert/oxidizing atmosphere. This procedure yielded Ni particles decorating the surface of a porous high surface area matrix, which presents a typical XRD pattern of aluminate structure. Ni particles are obtained with a homogeneous distribution over the surface and an average diameter of ca 25–30 nm. Obtained materials exhibit a high conversion of CO_2 below 500 °C, yielding CH_4 as a final product with selectivity >95%. The observed trend with the alkaline earth cation follows the order NiBaAlO-PRx > NiCaAlO-PRx > NiMgAlO-PRx. We propose that the high performance of the NiBaAlO sample is derived from both an appropriate distribution of Ni particle size and the presence of $BaCO_3$, acting as a CO_2 buffer in the process.

Keywords: heterogeneous catalysts; methanation; nickel nanoparticles; Sabatier reaction; carbon dioxide depletion

1. Introduction

The increasing use of fossil fuels during the last decades and its corresponding CO_2 emissions has incremented its concentration in the atmosphere, which has been associated with global climate change. Therefore, CO_2 emission diminution could be considered one of the major challenges today [1–4]. One strategy to face this issue is CO_2 valorization by its chemical reduction to value-added products. In particular, the catalytic hydrogenation of CO_2 for synthetic fuel production (methanol, dimethyl ether, methane) could be considered an economically viable solution, especially when CO_2 comes from industrial sources.

The Sabatier reaction ($4H_2 + CO_2 \rightarrow CH_4 + 2H_2O$) is an example of the power-to-gas process (P2G) [5–11]. In this process, exceeding electricity is utilized to electrolyze water, obtaining hydrogen and oxygen. H_2 is then combined with CO_2 to produce methane. When hydrogen is produced by renewable power sources, as in the example just mentioned, the synthetized methane may be considered "green", and the substitution of natural gas (fossil) results in an overall neutral CO_2 emission cycle [12–17].

The Sabatier reaction is highly exothermic, therefore, thermodynamically favored, although kinetically very slow ($\Delta H^0 = -164$ kJ/mol; $\Delta G^0 = -131$ kJ/mol), needing a catalyst to take place. The practical range of this reaction is restricted to 200–500 °C, as the reverse water gas shift reaction (RWGS) increases CO content at higher temperatures. Due to the exothermic character of the reaction and for large-scale applications, hot spots may occur in the catalytic bed, making it necessary to develop thermally stable catalysts to minimize aging.

A wide variety of noble metals (Rh, Ru, Pd) have been tested for the gas-phase hydrogenation of CO_2 into methane mediated by Sabatier's reaction in the gas phase under diverse conditions [18–22].

Ni-based catalysts are nowadays the most investigated metal due to its high activity, selectivity and lower cost compared with other alternatives [7,9,23–27] The performance of Ni-based catalysts depends, as in most of catalytic reactions, on metallic particle size, properties of the support (nature, basicity, reducibility) and the metal-support interaction [28–36]. In the case of Sabatier reaction, the performance of the catalyst may be inhibited by carbon deposition, what ultimately would decrease the conversion rate. Both factors depend mostly on Ni particle size.

It is generally accepted that the key intermediate of this reaction is the adsorbed formiate ($HCOO_{ad}$) specie [37], formed by the coadsorption of H_2 and CO_2. This format could either decompose on CO or be hydrogenated to CH_4. On small Ni particles with a low hydrogen coverage, CO formation is favored, while CH_4 formation is enhanced on bigger Ni particles. On the contrary, carbon formation is more favorable in big particles than in small particles. [16,38–45]. It is worth mentioning here that the adsorption of the formiate species would be favored on Brönsted basic sites due to the acid character of the CO_2 molecule.

In the present work, Ni-based nanosized particles have been formed on three different porous materials prepared by a two-step procedure, consisting of the decomposition of a precursor under inert gas at high temperatures, followed by a calcination step at a lower temperature. The resulting materials with a pseudo-hexaaluminate structure are used as precursors of the catalytic active phase, obtained from calcined materials under a reactant mixture ($H_2 + CO_2$) without any further pretreatment. The use of these aluminate-derived materials provided active, thermally stable, and very selective materials for the reduction of CO_2 with hydrogen (Sabatier reaction). The influence of the accompanying cation (Mg^{2+}, Ca^{2+}, Ba^{2+}) in the acid/basic character of the support and in the size of NiO particles is discussed.

2. Results

2.1. Textural Data and XRD of Calcined Samples

Table 1 compiles the main textural parameters (S_{BET} and porosity data) of the prepared catalysts together with two other samples prepared for comparison. These two samples correspond to a $NiBaAl_{11}O_{19}$ sample calcined directly in the air at 1000 °C (NiBaAlO-AIR) and a $NiBaAl_{11}O_{19}$ sample prepared as described elsewhere, with commercial carbon added in the preparation method and then calcined directly in the air [46] (NiBaAlO-Carbon). In this table, chemical analysis obtained by ICP is also included. The results obtained fit with the intended composition.

Table 1. Textural and chemical data of NiBaAlO, NiMgAlO, and NiCaAlO samples.

Sample	ICP Chemical Formula	BET Surface (m^2/g)	Pore Volume (cm^3/g)	Micropore Volume (cm^3/g)	Pore Size (Å)
NiBaAlO	$NiBa_{1.1}Al_{11}(O)_x$	30.0	0.11	0.002	12–17
NiMgAlO	$NiMg_{1.0}Al_{11}(O)_x$	58.0	0.20	0.005	14–17
NiCaAlO	$NiCa_{1.1}Al_{11}(O)_x$	31.0	0.21	0.003	22–24
NiBaAlO-AIR	$NiBa_{1.0}Al_{11}(O)_x$	7.2	0.02	1.6×10^{-4}	11–13
NiBaAlO-Carbon	$NiBa_{1.1}Al_{11}(O)_x$	15.0	0.03	6.3×10^{-4}	13–15

From these data is clear that the proposed preparation method results in a major increase in the S_{BET}, with more than a 5-fold increase with respect to the air calcined sample (NiBaAlO-AIR) and more than a 2-fold increase with respect to the NiBaAlO-carbon sample. This clearly indicates that samples prepared by the method described here showed higher porosity and specific surface area, parameters beneficial for higher catalytic activity.

The N_2 adsorption–desorption isotherms of catalysts (included in Supplementary Information) show that all the adsorption–desorption isotherms are qualitative of type IV (IUPAC classification) characteristic of porous materials [47,48]. The hysteresis with sharp adsorption and desorption branches in the P/P0 = 0.7–0.9 indicate a narrow mesopore size distribution.

Figure 1 shows the diffractograms of the three samples after their calcination in air at 600 °C. As can be seen, NiO is observed as a segregated phase, while the other elements form a mixed alkaline earth aluminate phase ($BaAl_2O_4$, $CaAl_4O_7$, and $MgAl_2O_4$). Some other trace phases can be detected for NiBaAlO and NiCaAlO (Al_2O_3 and NiC, respectively). The average crystallite domain size (calculated from the Scherrer formula) for the different detected phases is compiled in Table 2. Data in this table show that all the phases detected present an average crystallite domain of ca 25–40 nm, similar for all the samples, which reflects the repeatability of the preparation method, independently of the cation (Ba, Mg, Ca) incorporated into the aluminate structure. This small crystallite size is directly related to the preparation method, as deduced from the values obtained for the NiBaAlO-Air and NiBaAlO-Carbon samples, presenting values significantly higher in crystalline dominion. Therefore, the self-generated template induces a higher surface area, higher porosity, and smaller crystallite size, all parameters that are beneficial for the use of these materials as catalysts.
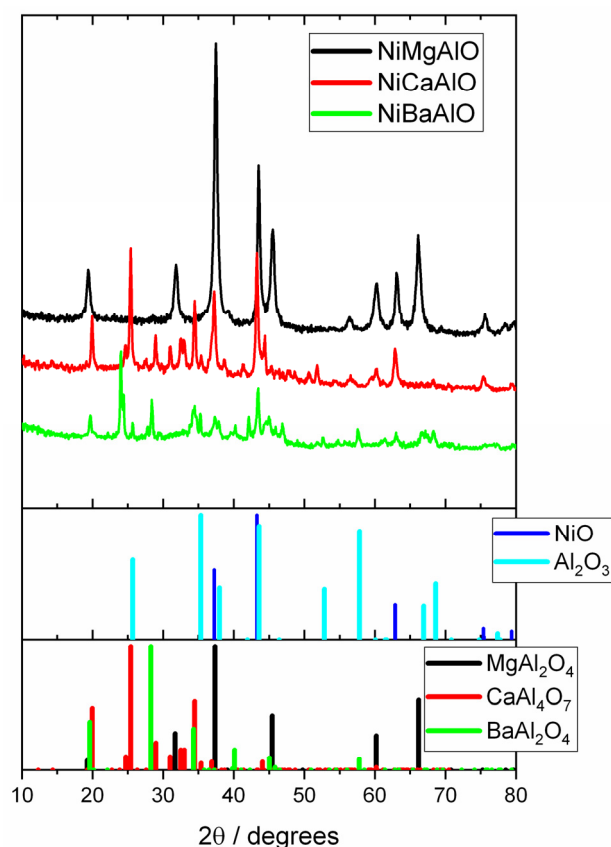

Figure 1. XRD Diffractograms of NiBaAlO, NiMgAlO, and NiCaAlO samples, where the main detected phases have been indicated (JCPDS: NiO = 01-073-1519; Al_2O_3 = 00-042-1468, $MgAl_2O_4$ = 00-001-157, $CaAl_2O_4$ = 00-017-0306).

Table 2. Crystallite size (diffraction dominion) calculated from Scherrer formula for NiBaAlO, NiMgAlO, and NiCaAlO samples.

	Crystallite Size Calculated from Scherrer Formula (nm)						
	NiBaAlO	**NiBaAlO-PRx**	**NiCaAlO**	**NiCaAlO-PRx**	**NiMgAlO**	**NiMgAlO-PRx**	**NiBaAlO-Carbon NiBaAlO-AIR**
NiO	23 ± 2	–	31 ± 2	–	24 ± 2	–	–
Metallic Ni	–	20 ± 2	–	30 ± 2	–	20 ± 2	–
Al_2O_3	35 ± 2	45 ± 2	–	–	–	–	–
$BaAl_2O_4$	30 ± 2	34 ± 2	–	–	–	–	63 ± 2 74 ± 2
$BaCO_3$	–	40 ± 2	–	–	–	–	–
$CaAl_4O_7$	–	–	24 ± 2	11 ± 2	–	–	–
$(MgAl_2O_4)$	–	–	–	–	15 ± 2	12 ± 2	–

2.2. Morphological and Micrographs of Calcined Samples (SEM/TEM)

Figure 2 presents SEM images of the typical morphology of the three samples. They are formed of large flakes that, in general, resemble a "cookie" form. The surface of these flakes is usually flat, although showing pores. On the contrary, the inner part of the "flakes" is highly porous, with a granular aspect with irregular particles of around 40–60 nm (Figure 2a). That size is in the order of magnitude of the crystallite domain size calculated from XRD, reflecting that most of the grains observed by SEM are frequently formed by single domains of the detected phases.
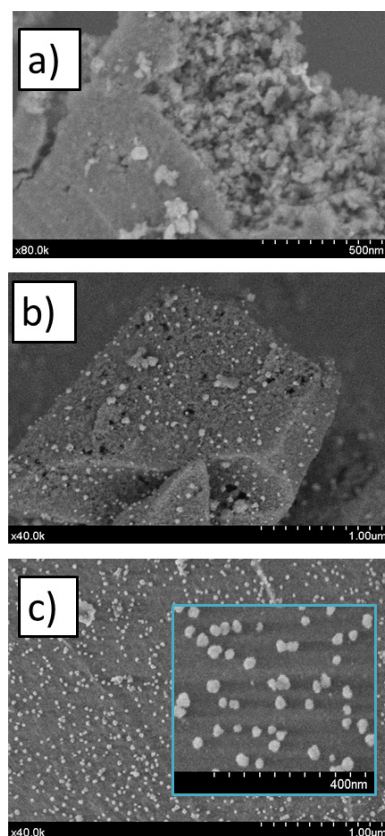
Figure 2. Scanning Electron microscopy images of (**a**) NiBaAlO, (**b**) NiCaAlO, and (**c**) NiMgAlO samples.

It is worth noting that some brighter particles are also observed in Figure 2b,c, homogeneously distributed onto the porous support. These particles, as confirmed by EDAXS, correspond to NiO. These NiO particles are well distributed on the surface of the flake aggregates of the oxidic phase ($BaAl_2O_4$, $CaAl_4O_7$, and $MgAl_5O_8$ –$MgAl_2O_4$) in the three catalysts, showing a narrow size distribution (ca 25–30 nm), similar to datum calculated from Scherrer formula.

Although smaller NiO particles have been suggested in some of the micrographs obtained would be difficult to observe by SEM due to the granular morphology of the samples and resolution limitation. In order to complement the SEM, TEM images of the samples have also been obtained. As an example of these images, Figure 3 shows details of NiBaAlO, NiCaAlO, and NiMgAlO samples, where besides the 25–30 nm NiO particles, much smaller NiO particles (ca. 5–7 nm) are clearly observed. It is worth noting that these small particles were not observed on SEM images (where only the surface of the particles is observed) and seemed to be incorporated into the structure of the oxidic material.
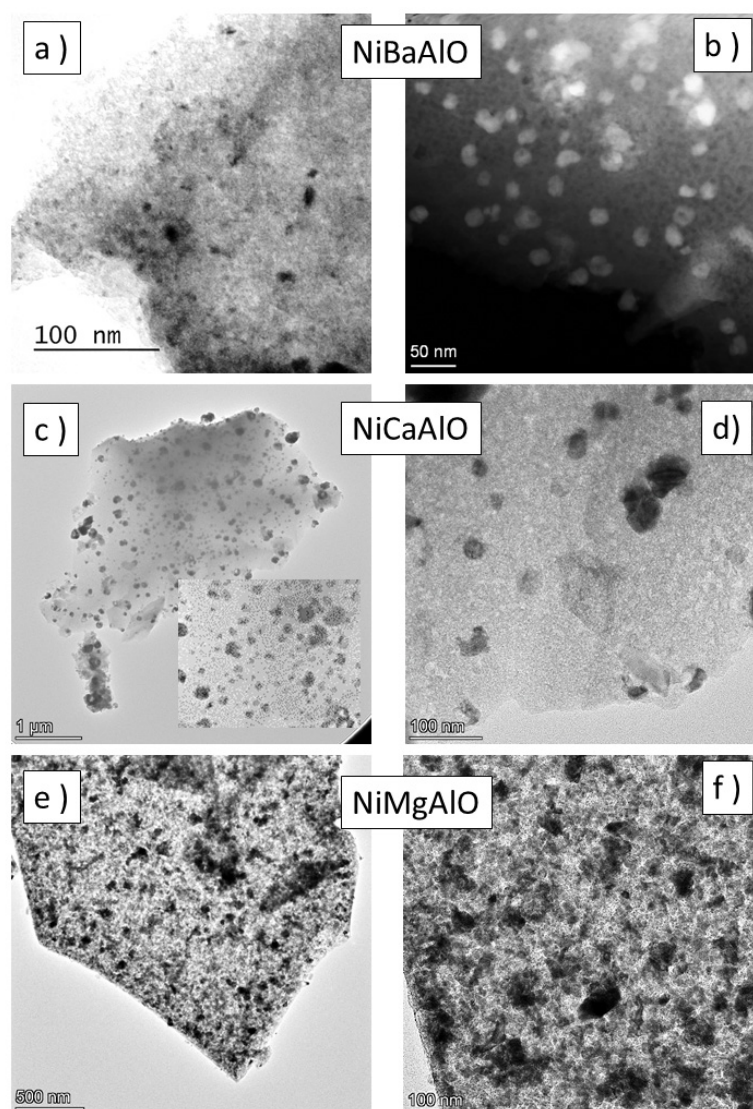

Figure 3. TEM images of (**a**,**b**) NiBaAlO, (**c**,**d**) NiCaAlO, and (**e**,**f**) NiMgAlO samples, where brighter/darker (depending on the type of field used) spots correspond to NiO particles.

2.3. Temperature-Programmed Reduction (TPR)

The TPR profiles obtained for the three samples are plotted in Figure 4. These TPR graphs show wide profiles, with a bimodal structure that can be divided into two zones:

623 K–873 K and 873 K–1173 K (maximum experimental temperature). The profiles in each zone present maxima at ca 723 K and 1073 K, although some shoulders are observed around those maxima. The adscription of these two zones in similar compounds have been discussed elsewhere [49,50], but still controversy remains in the literature: One hypothesis is that the low temperature peak is due to reduction of NiO particles, while the higher temperature peak is related to reduction of Ni^{2+} incorporated into the structure of an aluminate, perovskite, or similar structure. In our case, taking SEM/TEM images and XPS result, discussed later, we have been assigned to reduction of big and superficial NiO particles in the case of the lower temperature zone (623 K–873 K), while contribution of reduction at higher temperatures has been assigned to reduction of Ni^{2+} cations inside the structure [51] or reduction of very small particles cleaved inside the oxidic support [52]. It is worth noting that this bimodal assignation would fit with the observations made by SEM/TEM, where two particle sizes of NiO has been detected (20–30 nm and 5–7 nm). It is important also to note that these two particles seem to be arranged differently on the support: the bigger particles appear mostly on the surface of the aggregates being more accessible for their reduction, but, the smaller particles look to be clutched inside the oxidic matrix, what would difficult their process of reduction.
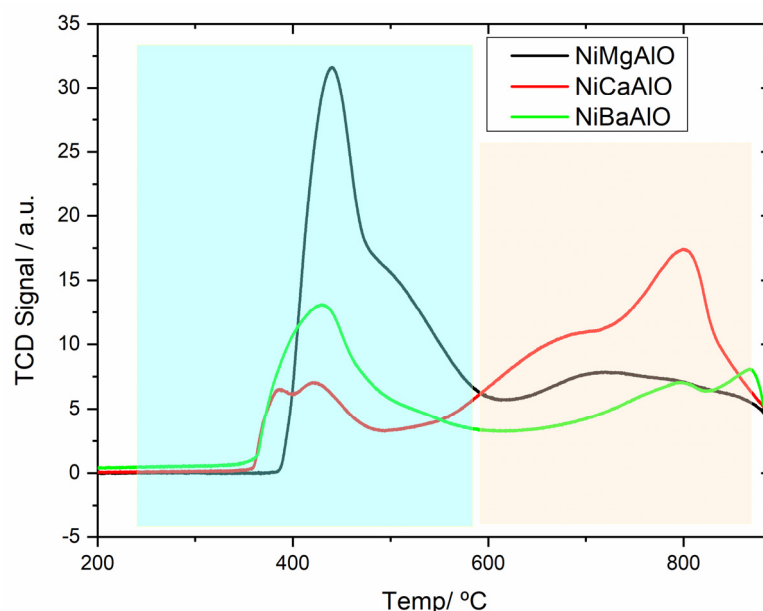
Figure 4. Temperature programmed reduction (TPR) profiles of the NiBaAlO, NiMgAlO, and NiCaAlO samples. Blue and pink windows reflect the two temperature ranges associated with the reduction processes described in the text.

2.4. X-ray Photoelectron Spectroscopy (XPS) of Calcined Samples

The chemical state and surface distribution of Ni species on the oxidic substrates were explored using XPS analysis (Figure 5, Tables 3 and 4). Two signals have been followed, especially due to their possible role in the reaction: Ni2p and C1s. In all the cases, the signals are plotted after normalization vs. the area of Al2p, also used as an internal reference for calibration (74.4 eV). XPS signals corresponding to the Ni2p levels present different satellite structures [53,54]. For Ni^{2+}, the satellite at about +6.0 eV might be assigned to a final state effect associated with a (core) $3d^8L$ configuration (where L stands for ligands), depending on the intensity and position of this satellite on factors such as bonding with ligands, symmetry, particle size and crystallinity [55,56].
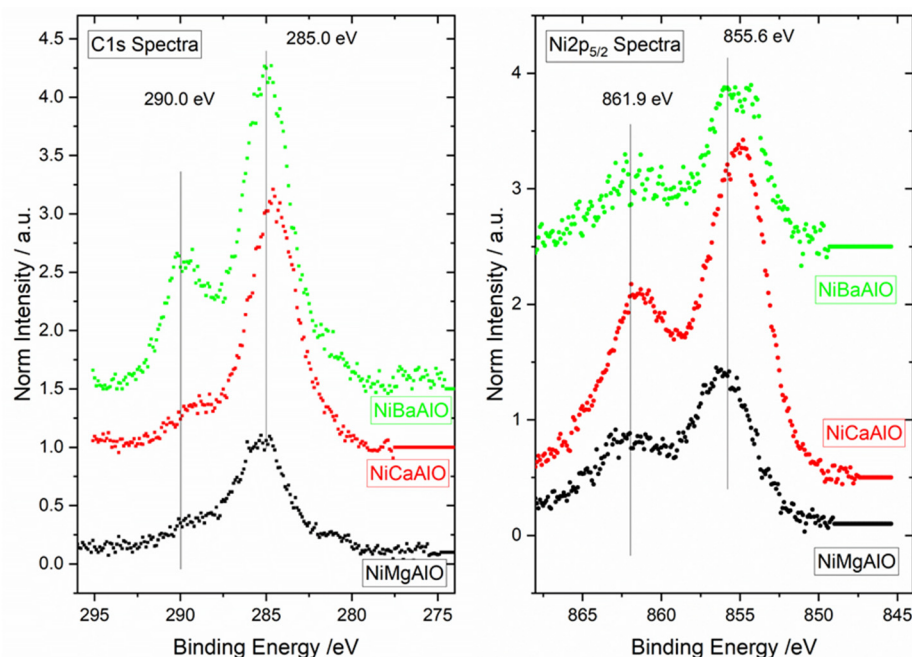
Figure 5. XPS spectra corresponding to the Ni2p$_{3/2}$ C1s and O1s regions of the NiBaAlO, NiMgAlO, and NiCaAlO calcined samples.

Table 3. Calculated surface % area obtained from XPS and peaks maxima for NiBaAlO, NiMgAlO, and NiCaAlO samples.

	Al2p	C1s	Ba3d	Ca2p	Mg1s	Ni2p	O1s
Areas and Maxima Binding Energies (eV) from XPS Zones							
	(B.E. eV)	(B.E. eV)	(B.E. eV)	(B.E. eV)	(B.E. eV)	(B.E. eV)	(B.E. eV)
NiBaAlO	38.9% (74.0 ± 0.1)	13.3% (284.7 ± 0.1)	2.5% (780.2 ± 0.1)			0.7% (854.3 ± 0.1)	44.6% (531.3 ± 0.1)
NiBaAlO-PRx	44.1% (74.0 ± 0.1)	4.7% (290.1 ± 0.1)	3.3% (780.8 ± 0.1)			0.5% (852.7 ± 0.1)	47.4% (531.7 ± 0.1)
NiCaAlO	43.0% (74.0 ± 0.1)	11.2% (284.6 ± 0.1)		1.7% (347.4 ± 0.1)		4.5% (854.8 ± 0.1)	39.7% (530.4 ± 0.1)
NiCaAlO-PRx	52.2% (74.0 ± 0.1)	3.3% (284.5 ± 0.1)		2.7% (348.0 ± 0.1)		3.1% (851.8 ± 0.1)	38.7% (531.5 ± 0.1)
NiMgAlO	40.6% (74.0 ± 0.1)	6.4% (285.3 ± 0.1)			2.1% (1303.5 ± 0.1)	1.3% (856.5 ± 0.1)	49.7% (531.4 ± 0.1)
NiMgAlO-PRx	44.1% (74.0 ± 0.1)	1.3% (281.5 ± 0.1)			2.1% (1304.2 ± 0.1)	1.2% (853.5 ± 0.1)	50.6% (532.2 ± 0.1)

In all three samples, the obtained spectra are quite similar in shape, but some differences in intensity are observed. The Ni2p$_{3/2}$ region reflects, in all cases, a shape typical of nickel oxide (main peak at 855.6 eV and a satellite at 862.1 eV), but the intensity in the NiCaAlO sample is about 2.5 times greater than for NiBaAlO and NiMgAlO sample (Table 3). It should be noted here that the intensity of a metallic particle dispersed onto a granular matrix, like the cases studied here, depends on several factors, namely: particle size of the metallic (NiO) and matrix phase (BaAl$_2$O$_4$, CaAl$_4$O$_7$, and MgAl$_5$O$_8$) [57] but also the surface/inner distribution of the NiO particles onto the oxidic matrix [52]. This may reflect, according to SEM images, that the NiCaAlO sample may present more NiO particles on the surface of the aluminate phase than the other two samples. The O1s in all the samples reflect a single peak centered at 531.1 eV, with no shoulder and quite similar intensity, according to the similar stoichiometry found from XRD for the aluminate phases found in the three samples. The C1s spectra of the samples present in all the cases a

major peak, centered at ca. 285.0 eV (due to adventitious carbon) and a shoulder at higher binding energy (290.0 eV), more noticeable in the case of NiBaAlO sample, as can be easily visualized in data compiled in Table 4 (a visualization of the fitting of these signals have been incorporated as Supplementary Information). These shoulders at high binding energy correspond with carbonates and/or oxy-hydroxyl species on the surface of the support.

Table 4. Calculated surface % area for the indicated elements obtained from XPS and peaks maxima for NiBaAlO, NiMgAlO, and NiCaAlO samples.

	Percentage of Indicated Species for Deconvolution of C1s and Ni2p XPS Signals				
	C1s-1% (Carbonate)	C1s-2% (Graphitic)	C1s-3% (Carbide)	Ni2p-1% (Ni^{2+})	Ni2p-2% (Ni^0)
NiBaAlO	25.3	69	5.7	90.0	10.0
NiBaAlO-PRx	45.9	38.6	15.5	62.7	37.3
NiCaAlO	10.7	84.6	4.8	98.7	1.3
NiCaAlO-PRx	22.8	50.3	26.9	50.6	49.4
NiMgAlO	15.3	77	7.6	100.0	0.0
NiMgAlO-PRx	3.3	48.1	48.6	69.5	30.5

2.5. Catalytic CO_2 Hydrogenation

The catalytic conversion of CO_2 and selectivity versus CO and CH_4 corresponding to the NiBaAlO, NiMgAlO, and NiCaAlO are plotted in Figure 6.
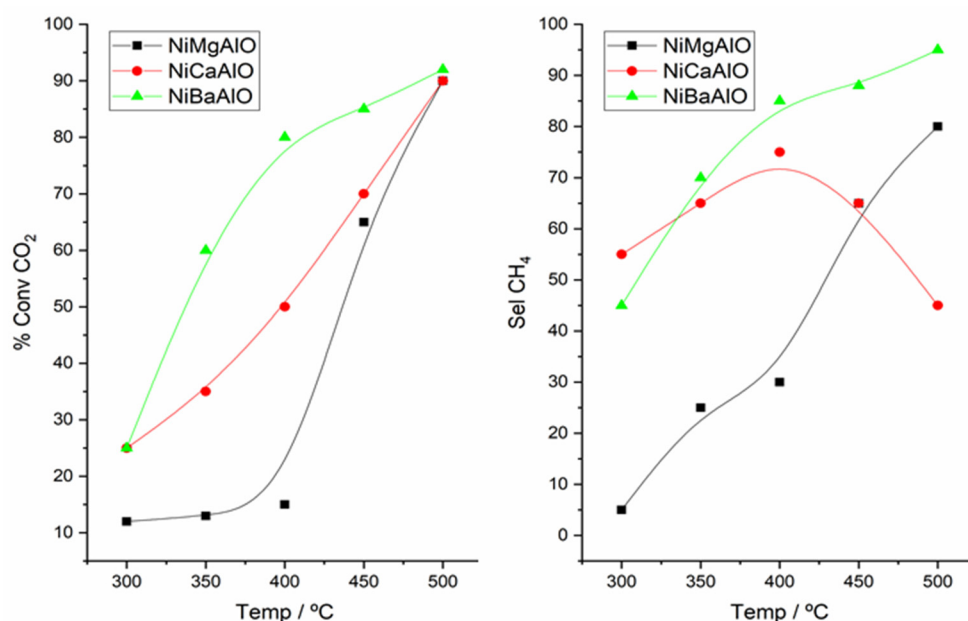
Figure 6. Conversion of CO_2 (**left**) and selectivity toward CH_4 (**right**) for NiBaAlO, NiMgAlO, and NiCaAlO calcined samples.

It should be remarked that CH_4 and CO were the only products of the reaction detected and, therefore, CO selectivity is complementary to CH_4 for 100% (water product is condensed in a cold trap before entering into the GC). As explained in the experimental section, samples are heated up to 500 °C at different steps and then cooled down, taking reaction data both in the heating ramp and in the cooling down section. Although, in general, conversion and selectivity values do not differ more than 5–10% between these two stages, only data corresponding to the cooling down steps have been taken into consideration.

The results show an increased conversion rate in all the samples above 300 °C, especially abrupt in the case of the NiBaAlO sample, which reaches 80% conversion at 400 °C and ca. 95% at 500 °C. The NiCaAlO sample increases its conversion also with temperature, but its variation is more linear. On the other hand, the NiMgAlO sample shows a small conversion between 300 °C and 400 °C and only increases above this temperature. Nevertheless, at 500 °C, all the catalysts reach a conversion of ca. 95%. It should be mentioned here that the reactants are diluted in He and that, according to the stoichiometry, during the reaction, there is a decrease in the number of moles produced with respect to the moles consumed, which may modify slightly the apparent concentration of products as detected by GC (the condensation of water by a cold trap also helps in this direction), making that some of the conversions and selectivities appear a bit higher than real values, with values slightly above to the thermodynamic values, which do not affect the main conclusions of this study. The selectivity toward CH_4 follows a similar trend: NiBaAlO is the sample that presents higher selectivity (85–95% at 400–500 °C) and at lower temperatures, followed by the sample NiCaAlO with a big difference in the range 400- 500 °C (25–80%). Finally, the NiMgAlO sample only presents significant conversions above 450 °C, but the selectivity decrease in this range of temperature.

Together with the characterization of the samples before the reaction, we have performed an analysis of post-reaction samples (labeled with the suffix—PRx, i.e., NiBaAlO-PRx and so on), which is presented below. In the case of XPS, this analysis has been performed using an "in situ" reaction chamber that avoids exposure of samples to the atmosphere, and the thermal treatment has been performed using the same gas composition and flows as that used for catalytic tests, as explained in the experimental section. This "in situ" treatment ensures that the XPS analysis of the post-reaction sample is not contaminated by exposition to the atmosphere, which would especially affect carbon signals and nickel oxidation state.

### 2.6. Textural Data and XRD of Post-Reaction Samples

XRD of post-reaction samples is shown in Figure 7. Several aspects are relevant: In the case of NiBaAlO-PRx, Nickel is observed as metallic Ni, and the formation of $BaCO_3$ is observed. In the case of NiCaAlO-PRx, Ni is also found as a metallic phase, and the $CaAl_4O_7$ remains unaltered. Nevertheless, in NiMgAlO-PRx, nickel is found as a mixture of metallic and NiO phases.
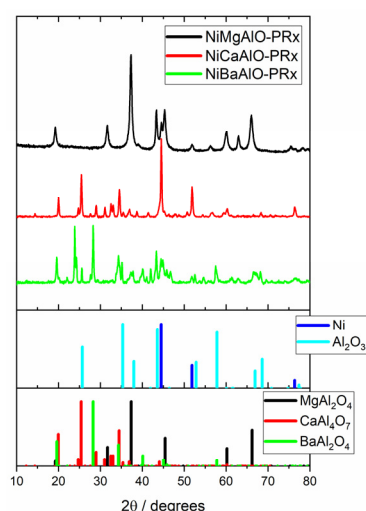
Figure 7. XRD Diffractograms of NiBaAlO-PRx, NiMgAlO-PRx, and NiCaAlO-PRx samples, where main phases detected have been indicated (JCPDS: Ni = 01-087-0712; Al_2O_3 = 00-042-1468, $MgAl_2O_4$ = 00-001-157, $CaAl_2O_4$ = 00-017-0306).

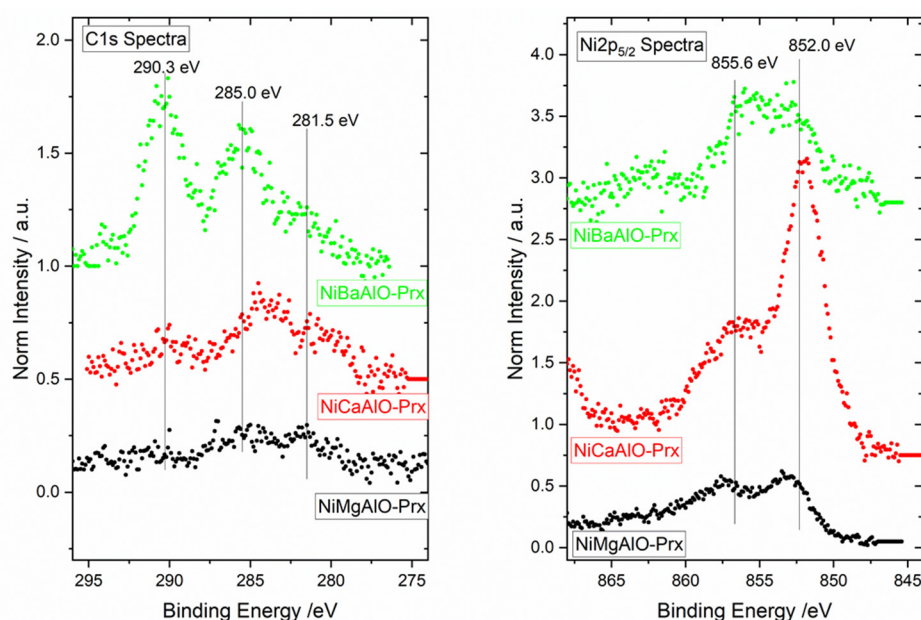*2.7. SEM/TEM of Post-Reaction Samples*

The SEM images of post-reaction samples can be seen in Figure 8. Again, and for simplicity, only one image of each sample is reproduced, but similar images can be found on each sample. Images on the right and center show that the "cookie" morphology is conserved, and no significant changes were detected for the grain size of oxidic support. Carbon filament or deposits were not detected for any sample. In the case of Ni particles deposited on the surface of the "flakes", a small increase in size was detected with an average diameter of ca. 30–40 nm and a more rounded shape. In the case of NiBaAlO-PRx sample (c), we have observed the appearance of some type of "spikes" on the surface of the aggregates. An EDAX analysis of these zones shows that they are formed by C, O, and Ba. These "spikes" were observed neither on the NiCaAlO-PRx nor on the NiMgAlO-PRx.
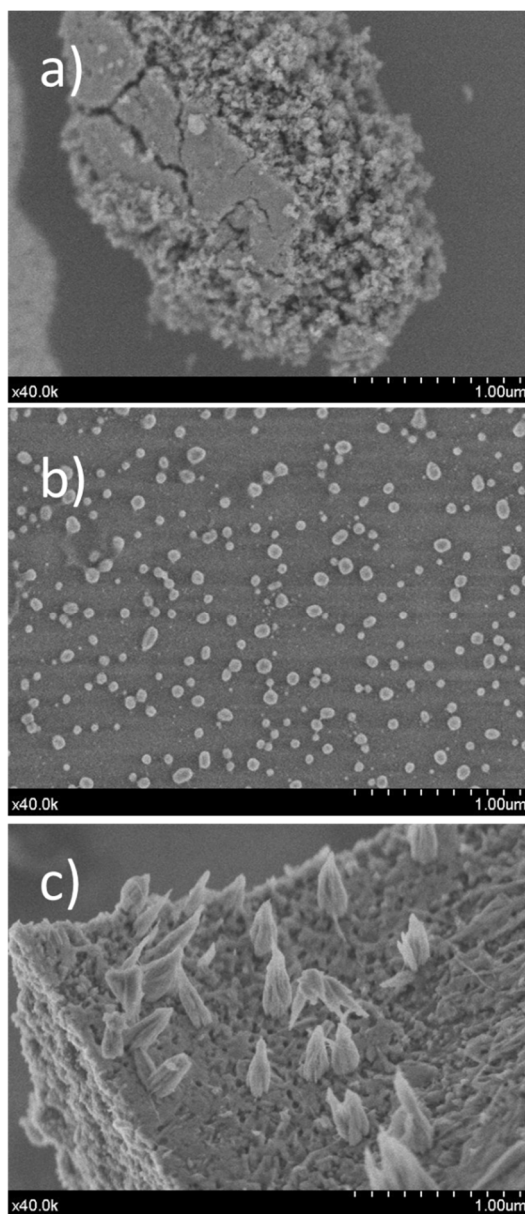
Figure 8. SEM images of post-reaction samples: (**a**) of NiCaAlO-PRx (TOP), (**b**) NiMgAlO-PRx (MIDDLE), and (**c**) NiBaAlO-PRX (BOTTOM).

2.8. "In Situ" XPS Analysis of Post-Reaction Samples

Figure 9 shows XPS spectra of post-reaction samples, corresponding to $Ni2p_{3/2}$ and C1s regions. In the case of $Ni2p_{3/2}$, the signals for NiCaAlO-PRx and NiMgAlO-PRx show a maximum at 851.8 eV and a shoulder at 856.1 eV. The spectrum of NiBaAlO-PRx depicts a broad shape, with two bumps at approximately the same positions as the other two samples (851.8 eV, 856.1 eV). The position of a maximum at ca. 851.8 eV is indicative of the presence of metallic Ni. Although bulk Ni^0 has a very small satellite intensity vs. the main peak, the intensity ratio of satellite/main peak has been discussed long ago as a function of Ni particle size and interaction with the support [57]. The observed satellite/main peak ratio is observed to proceed in the order NiBaAlO-PRx > NiMgAlO-PRx > NiCaAlO-PRx. The position of the main peak is also slightly shifted to higher binding energies in the order NiBaAlO-PRx > NiMgAlO-PRx > NiCaAlO-PRx. A fitting of these signals has been performed using the same shapes for all three samples, which results have been summarized in Table 4. (fitting has been included in Supplementary Materials). The results of this fitting show that the percentage of metallic Ni varies NiCaAlO-PRx < NiBaAlO-PRx < NiMgAlO-PRx.

Figure 9. XPS spectra corresponding to the $Ni2p_{3/2}$ and C1s regions of the NiBaAlO-PRx, NiMgAlO-PRx, and NiCaAlO-PRx post-reaction samples.

The C1s signals of the three samples present big differences with respect to the calcined samples (see Tables 3 and 4). The first remarkable fact is the abrupt diminution of the C1s signal due to the elimination during the reaction of the adventitious C1s signal found in the original samples. The amount of total carbon in the samples follows the trend NiBaAlO-PRx > NiCaAlO-PRx > NiMgAlO-PRx. In the case of NiMgAlO-PRx and NiCaAlO-PRx, a new peak at 280.6 eV was observed. This peak has been usually assigned to Ni_3C or NiC_x [58–61]. On the contrary, in the case of NiBaAlO-PRx, the more intense peak is centered at ca. 289.4 and 285.0 eV, which can be ascribed to $BaCO_3$ and graphitic carbon. There is also a small shoulder at 284.0 eV, which could be associated with a small contribution of NiC but with much lower intensity than in the case of NiMgAlO-PRx and NiCaAlO-PRx. A more comprehensive summary is compiled in Table 4, showing that the carbonate peak (289.4 eV) follows the trend NiBaAlO-PRx > NiCaAlO-PRx > NiMgAlO-PRx, while the nickel carbide peak presents the opposite tendency: NiBaAlO-PRx < NiCaAlO-PRx < NiMgAlO-PRx.

3. Discussion

Ni/NiO nanosized particles have been formed on different oxidic supports ($BaAl_2O_4$, $CaAl_4O_7$, and $MgAl_5O_8$) through a simple and non-expensive method, consisting of thermal decomposition of a precursor derived from citric acid and metallic salts of Ni, Ba, Mg, and Ca. The obtained catalysts show a porous structure, with a higher specific surface area than others with similar composition, forming aggregates with a "cookie" morphology. NiO particles are observed evenly distributed on that "cookie" morphology. From TPR AND SEM/TEM data, we can conclude that NiO/Ni particles are deposited on the surface of the support, with a mean diameter of ca. 20–30 nm (Ni_{d25}), but also on the inner structure of the aggregates, with a much smaller size, ca. 5–7 nm (Ni_{d5}). That would be in accordance with the recent DFT studies that have calculated that the TOF for CO_2 hydrogenation presents a maximum on very small particles (ca 2–3 nm) [37].

The presence of a segregated NiO phase instead of a pure $NiMAl_{11}O_{19}$ hexaaluminate phase is probably due to an insufficient temperature of crystallization. In fact, we have observed the formation of such phase ($NiBaAl_9O_{11}$) when the precursor is calcined in air at 1400 °C, but at the expense of a severe specific surface area loss. In any case, that does not result in a limitation on the catalysts' performance, as shown here. In any case, the NiO is transformed during heating in the reaction mixture into a metallic nickel phase (Ni^0), with only a small increase in size, both for small particles and bigger ones.

Analysis of XPS intensity of $Ni2p_{3/2}$ signals and TPR areas of low/high temperature of reduction in calcined samples indicate that the proportion of Ni_{d5}/Ni_{d25} depends on the alkaline earth cation, in the order NiMgAlO-PRx < NiCaAlO-PRx < NiBaAlO-PRx. Nevertheless, chemical analysis has shown that Ni content is the same in all the samples (as per mol of sample). Considering that the average size (and shape) of Ni bigger particles is the same in all the samples, let us discard that the differences observed could be related to different Ni facets and, therefore, pathways of reaction associated with this [62].

Finally, C1s of post-reaction samples show the formation of nickel carbide species on NiMgAlO-PRx and NiCaAlO-PRx samples and at a lower degree on NiBaAlO-PRx samples. Two more factors should be considered to explain the differences observed in catalytic performance: the presence of carbide and carbonate species. In this context, it is worth noting that carbide species have been recently proposed as an appealing alternative for different processes, as CO_2 hydrogenation [63] in metals such as Mo, Ru, etc., and more recently have been discussed, based on micro-kinetic simulations, found that for Ni particles, the dominant kinetic route for CO_2 hydrogenation corresponds to a combination of the carbide and formate reaction pathways [37]. On the other hand, carbonate species are more favored in NiBaAlO-PRx than in NiCaAlO-PRx and NiMgAlO-PRx. It is worth noting here that catalytic performance follows the same tendency NiMgAlO-PRx < NiCaAlO-PRx < NiBaAlO-PRx. The influence of basicity of support and, in particular, the formation of carbonates have been proposed as an alternative pathway for the Sabatier reaction [35,64].

We propose that the high performance of the NiBaAlO sample is a consequence of the higher contribution of small particles and the basicity of the Ba-aluminate phase that is acting as support. In particular, the formation of $BaCO_3$ crystals, detected by SEM and XPS, would act a buffer in the process of adsorption and transfer of CO_2 to the Ni particles (via adsorbed formiate species). That basicity would be enhanced with larger cations, such as Ba or Ca, and less favored for the Mg cation. On the contrary, carbon deposits on Ni particles, either as graphitic or carbide species, mostly found on Mg samples, would inhibit the performance of formiate species and enhance CO formation.

4. Materials and Methods

4.1. Preparation of the Catalysts

Catalysts here used have been prepared using hexaaluminate-derived materials as precursors of the final materials; basically, NiO particles deposited onto a $M^{2+}Al_2O_4$ phase (M^{2+} = Mg, Ca, Ba). All samples were prepared by a modification of the preparation method described elsewhere [65], adjusting the stoichiometry to obtain $NiMAl_{11}O_{19}$ (M = Ca, Ba,

Mg) instead of $NiAl_2O_4$ reported in the cited work. This preparation method allows wide flexibility of composition and low impurities when easily decomposable salts are used, such as nitrates or ammonium metal compounds. In a typical preparation procedure, several stages are comprised: (a) dissolution; (b) formation of gel and drying; (c) decomposition in inert gas of dried gel; (d) calcination and removal of carbonaceous species (e) direct reduction of samples under reaction mixture ($H_2 + CO_2$) atmosphere. In the dissolution stage, appropriate quantities of corresponding nitrates ($Mg(NO_3)_2$ (Aldrich), $Ca(NO_3)_2 \cdot$, $Ba(NO_3)_2 \cdot 6H_2O$ (Aldrich) $Al(NO_3)_3 \cdot 9H_2O$ and $Ni(NO_3)_2 \cdot 6H_2O$ were dissolved in excess of deionized (MilliQ quality) water. Amounts of these salts were appropriate to provide a final formula $NiBaAl_{11}O_{19}$, $NiCaAl_{11}O_{19}$, and $NiMgAl_{11}O_{19}$. Citric acid (Aldrich) was added in excess (100 wt.%) over the stoichiometric quantity to ensure both a complete complexation of the metal ions and an excess of the carbonaceous amount in the decomposition stage. Once the dissolution was complete, water was evaporated on a rotavapor up to 313 K leading to the apparition of a viscous spongy gel. This gel is dried overnight in an oven at 393 K. During this treatment, a foam is produced, resulting from gas bubbles coming from the partial decomposition of nitrates and citric acid. At this stage, classic citrate methods normally include calcination under oxygen or air at temperatures between 973 and 1273 K. In our method, we have introduced a modification, and the thermal treatment is performed under a constant flow of inert gas atmosphere using a low heating ramp (1–5K/min) up to 1373 K. After this treatment, a composite of carbonaceous species and well-formed aluminate-precursor particles is obtained. The presence of the carbonaceous species partially inhibits the sintering of the aluminates particles (carbonaceous template) during the high-temperature treatment, but the high temperature used helps a well-crystallized phase. Further thermal treatment with air at lower temperatures (typically 600–700 °C) allows the complete removal of the carbonaceous species, leaving a porous structure in the sample with a much higher specific surface area than that obtained without the carbonaceous template step. After this calcination step, the obtained materials, with the stoichiometry described above in this paragraph, will be denoted NiBaAlO, NiMgAlO, and NiCaAlO. It is important to note here that calcined samples are not the active phase, and further reducing treatment is needed to decompose this aluminate structure with the formation of Ni metallic nanoparticles. Thermal decomposition of these precursors under a reactant mixture leads to Ni nanoparticles deposited on an alkaline earth aluminate of high homogeneity.

4.2. Catalytic Test

Catalytic tests were performed over 200 mg of catalyst held between two pompons of quartz glass in a tubular quartz reactor. Samples were pre-dried in an oven at 120 °C and sieved to obtain particles with size <100 μm prior to their introduction in the reactor. No further treatment was applied to the samples prior to contact with the reaction mixture ($H_2:CO_2:He = 40:10:50$ mL/min). The reaction was carried out at 300, 350, 400, 450, and 500 °C steps for two hours, with a heating ramp of 5 °C/min between plateaus. After being heated at the maximum temperature for 2 h, samples were cooled down with the same temperature steps (450, 400, 350, and 300 °C). It is worth noting here that due to the high conversion rate observed, an axial gradient along the bed length could occur. In that context, we have performed a simulation using the "gradientcheck" tool (https://engineering.purdue.edu/~catalyst/ (accessed on 15 December 2022)) with the parameters used in this work, and while there is a noticeable gradient in the radial direction, there could be a gradient of ca. 5 °C along the axial direction. Nevertheless, additional tests using the same amount of catalysts mixed with SiC as a diluent have not shown significant changes in the conversion/selectivity obtained. Products were analyzed by gas chromatography using a VARIAN GC3800 GC equipment, connected online with the reactor, provided with two columns Porapak, molecular Sieve) and TCD detectors. A water cold trap formed by a siphon cooled down by a Peltier cooler (ca. 1–3 °C) was used before the entrance to the GC, avoiding saturation of the columns and TCD damage. To assess

the catalytic activity, the CO_2 conversion X (%), and CH_4 selectivity S (%) by using the following formulas:

$$CO_2 \text{ conversion } (\%) = \frac{[CO_2]_{in} - [CO_2]_{out}}{[CO_2]_{in}} \times 100$$

$$CH_4 \text{ selectivity } (\%) = \frac{[CH_4]}{[CO_2]_{in} - [CO_2]_{out}} \times 100$$

where $[F]_{in}$ and $[F]_{out}$ are the volume concentration of CO_2 and/or CH_4 at the inlet and outlet, respectively.

4.3. N_2-Physisorption

N_2 adsorption/desorption isotherms were obtained at −196 °C in a TRISTAR II (Micromeritics) equipment. With a minimum amount of 50 mg. Samples were pre-treated under vacuum at 150 °C prior to the adsorption/desorption experiment. Surface areas and porosity were calculated according to the BET and BJH methods, respectively.

4.4. SEM/TEM

SEM images were obtained in a Hitachi S-5200 microscope with a field emission filament, using an accelerating voltage of 4–5 kV and an extraction current of 10 mA. Transmission electron microscopy was carried out in a Philips CM200 microscope operating at 200 kV. In both cases, samples were deposited onto a copper grid coated with lacey carbon. Analysis of particle size was performed by sampling 100 particles.

4.5. XRD

Diffractogram patterns of calcined and reduced samples were obtained in a PANalytical X-Pert PRO diffractometer with a Cu anode (λ = 1.5418 Å, Cu Kα), using a Bragg-Brentano configuration in the 2θ range of 10–80°, with a step of 0.05° and an effective acquisition time of 240 s.

4.6. TPR

Temperature-programmed reduction experiments were performed using a thermal conductivity detector calibrated with a commercial NiO. An estimated amount of calcined sample for consuming 100 μmol of H_2 was used in each case. Conventional experiments were carried out from room temperature up to 1000 °C with a heating ramp of 10 °C min^{-1}. Experimental conditions were chosen to avoid peak overlapping [66].

4.7. XPS

Studies were performed in a customized system incorporating a hemispherical analyzer (SPECS Phoibos 100) and a non-monochromatized X-ray source (Al Kα; 1486.6 eV, Mg Kα, 1253.6 eV). The analyzer was operated at a fixed transmission and 50 eV pass energy with an energy step of 0.1 eV. Binding energies were calibrated using C1s or Al2p (284.6 eV or 74.0 eV) as an internal reference. Prior to each analysis, samples were evacuated to 10^{-9} mbar at room temperature. The "in situ" treatments were performed on a high-pressure, high-temperature commercial cell (SPECS HPC) coupled to the main chamber of the spectrometer. The high-temperature, high-pressure cell design allows sample heating up to 800 °C, under flow or static conditions, at pressures up to 20 bar or dynamic flows in the range 20–500 NmL·min^{-1}. This arrangement enabled a transfer of post-reaction samples from the reaction chamber to the spectrometer under UHV conditions, avoiding exposure to the laboratory atmosphere. In a typical experiment, the sample was initially placed in the sample holder (in the form of a pelletized disc) and transferred to the spectrometer chamber, where XPS spectra were acquired. The sample was then transferred under vacuum to the high-pressure cell, where it was exposed to the reactive gases and heated to the appropriate temperature. The flow and concentration of gases (CO_2 + H_2) were the same as those

used for catalytic testing (vide infra). After the treatment, the sample was cooled to room temperature under the same reaction atmosphere, evacuated down to 10^{-7} mbar in less than two minutes, and then transferred back to the spectrometer chamber for analysis, avoiding ambient exposure. This allows us to analyze the surface and chemical state of the elements exposed at the surface of the catalysts after reaction conditions.

Supplementary Materials: The following supporting information can be downloaded at: https: //www.mdpi.com/article/10.3390/catal13010142/s1, Figure S1: Nitrogen adsorption–desorption isotherms of catalysts. Table S1: Calculated surface % area for the indicated elements obtained from XPS and peaks maxima for NiBaAlO, NiMgAlO, and NiCaAlO samples. Table S2: List of main diffraction peaks and planes for detected phases.

Data Availability Statement: Data are contained within the article and in the provided Supplementary Materials.

Conflicts of Interest: The authors declare no conflict of interest.

References

1. International Energy Agency. *World Energy Outlook*; OECD/IEA: Paris, France, 1995.
2. *BP Energy Outlook*; 2019 Edition; BP: London, UK, 2019.
3. Höök, M.; Tang, X. Depletion of fossil fuels and anthropogenic climate change—A review. *Energy Policy* **2013**, *52*, 797–809. [CrossRef]
4. Olah, G.A. Beyond Oil and Gas: The Methanol Economy. *Angew. Chem. Int. Ed.* **2005**, *44*, 2636–2639. [CrossRef] [PubMed]
5. Meylan, F.D.; Moreau, V.; Erkman, S. Material constraints related to storage of future European renewable electricity surpluses with CO_2 methanation. *Energy Policy* **2016**, *94*, 366–376. [CrossRef]
6. Reiter, G.; Lindorfer, J. Evaluating CO_2 sources for power-to-gas applications–A case study for Austria. *J. CO_2 Util.* **2015**, *10*, 40–49. [CrossRef]
7. Rönsch, S.; Schneider, J.; Matthischke, S.; Schlüter, M.; Götz, M.; Lefebvre, J.; Prabhakaran, P.; Bajohr, S. Review on methanation–from fundamentals to current projects. *Fuel* **2016**, *166*, 276–296. [CrossRef]
8. Schiebahn, S.; Grube, T.; Robinius, M.; Tietze, V.; Kumar, B.; Stolten, D. Power to gas: Technological overview, systems analysis and economic assessment for a case study in Germany. *Int. J. Hydrogen Energy* **2015**, *40*, 4285–4294. [CrossRef]
9. Stangeland, K.; Kalai, D.; Li, H.; Yu, Z. CO_2 Methanation: The Effect of Catalysts and Reaction Conditions. *Energy Procedia* **2017**, *105*, 2022–2027. [CrossRef]
10. Bengaouer, A.; Bedel, L. 20. CO_2 hydrogenation to methane. In *Volume 2 Transformations*; De Gruyter: Berlin, Germany, 2019; pp. 385–412.
11. Sterner, M.; Specht, M. Power-to-Gas and Power-to-X—The History and Results of Developing a New Storage Concept. *Energies* **2021**, *14*, 6594. [CrossRef]
12. Li, K.; An, X.; Park, K.H.; Khraisheh, M.; Tang, J. A critical review of CO_2 photoconversion: Catalysts and reactors. *Catal. Today* **2014**, *224*, 3–12. [CrossRef]

13. Wang, L.; Ghoussoub, M.; Wang, H.; Shao, Y.; Sun, W.; Tountas, A.A.; Wood, T.E.; Li, H.; Loh, J.Y.Y.; Dong, Y.; et al. Photocatalytic Hydrogenation of Carbon Dioxide with High Selectivity to Methanol at Atmospheric Pressure. *Joule* **2018**, *2*, 1369–1381. [CrossRef]

14. Wang, Y.; Zhao, J.; Li, Y.; Wang, C. Selective photocatalytic CO_2 reduction to CH_4 over Pt/In_2O_3: Significant role of hydrogen adatom. *Appl. Catal. B Environ.* **2018**, *226*, 544–553. [CrossRef]

15. Yaashikaa, P.R.; Kumar, P.S.; Varjani, S.J.; Saravanan, A. A review on photochemical, biochemical and electrochemical transformation of CO_2 into value-added products. *J. CO_2 Util.* **2019**, *33*, 131–147. [CrossRef]

16. Zhang, F.; Li, Y.-H.; Qi, M.-Y.; Tang, Z.-R.; Xu, Y.-J. Boosting the activity and stability of $Ag-Cu_2O/ZnO$ nanorods for photocatalytic CO_2 reduction. *Appl. Catal. B Environ.* **2019**, *268*, 118380. [CrossRef]

17. Rozzi, E.; Minuto, F.; Lanzini, A.; Leone, P. Green synthetic fuels: Renewable routes for the conversion of non-fossil feedstocks into gaseous fuels and their end uses. *Energies* **2020**, *13*, 420. [CrossRef]

18. Karelovic, A.; Ruiz, P. Mechanistic study of low temperature CO_2 methanation over Rh/TiO_2 catalysts. *J. Catal.* **2013**, *301*, 141–153. [CrossRef]

19. Petala, A.; Panagiotopoulou, P. Methanation of CO_2 over alkali-promoted Ru/TiO_2 catalysts: I. Effect of alkali additives on catalytic activity and selectivity. *Appl. Catal. B Environ.* **2018**, *224*, 919–927. [CrossRef]

20. Vogt, C.; Monai, M.; Kramer, G.J.; Weckhuysen, B.M. The renaissance of the Sabatier reaction and its applications on Earth and in space. *Nat. Catal.* **2019**, *2*, 188–197. [CrossRef]

21. Xu, J.; Su, X.; Duan, H.; Hou, B.; Lin, Q.; Liu, X.; Pan, X.; Pei, G.; Geng, H.; Huang, Y. Influence of pretreatment tem-perature on catalytic performance of rutile TiO_2-supported ruthenium catalyst in CO2 methanation. *J. Catal.* **2016**, *333*, 227–237. [CrossRef]

22. Panagiotopoulou, P. Hydrogenation of CO_2 over supported noble metal catalysts. *Appl. Catal. A Gen.* **2017**, *542*, 63–70. [CrossRef]

23. Frontera, P.; Macario, A.; Ferraro, M.; Antonucci, P. Supported Catalysts for CO_2 Methanation: A Review. *Catalysts* **2017**, *7*, 59. [CrossRef]

24. Özdemir, H.; Öksüzömer, M.F.; Gürkaynak, M.A. Preparation and characterization of Ni based catalysts for the catalytic partial oxidation of methane: Effect of support basicity on H_2/CO ratio and carbon deposition. *Int. J. Hydrogen Energy* **2010**, *35*, 12147–12160. [CrossRef]

25. Stangeland, K.; Kalai, D.Y.; Li, H.; Yu, Z. Active and stable Ni based catalysts and processes for biogas upgrading: The effect of temperature and initial methane concentration on CO_2 methanation. *Appl. Energy* **2018**, *227*, 206–212. [CrossRef]

26. Tsiotsias, A.I.; Charisiou, N.D.; Yentekakis, I.V.; Goula, M.A. Bimetallic Ni-Based Catalysts for CO_2 Methanation: A Review. *Nanomaterials* **2020**, *11*, 28. [CrossRef] [PubMed]

27. Wang, G.; Zhang, S.; Zhu, X.; Li, C.; Shan, H. Dehydrogenation versus hydrogenolysis in the reaction of light alkanes over Ni-based catalysts. *J. Ind. Eng. Chem.* **2020**, *86*, 1–12. [CrossRef]

28. Kwak, J.H.; Kovarik, L.; Szanyi, J. Heterogeneous Catalysis on Atomically Dispersed Supported Metals: CO_2 Reduction on Multifunctional Pd Catalysts. *ACS Catal.* **2013**, *3*, 2094–2100. [CrossRef]

29. Wu, Z.; Ge, S.; Zhang, M.; Li, W.; Tao, K. Synthesis of nickel nanoparticles supported on metal oxides using electroless plating: Controlling the dispersion and size of nickel nanoparticles. *J. Colloid Interface Sci.* **2009**, *330*, 359–366. [CrossRef]

30. Azancot, L.; Bobadilla, L.F.; Santos, J.L.; Córdoba, J.M.; Centeno, M.A.; Odriozola, J.A. Influence of the preparation method in the metal-support interaction and reducibility of Ni-Mg-Al based catalysts for methane steam reforming. *Int. J. Hydrogen Energy* **2019**, *44*, 19827–19840. [CrossRef]

31. Damyanova, S.; Pawelec, B.; Palcheva, R.; Karakirova, Y.; Sanchez, M.C.; Tyuliev, G.; Gaigneaux, E.; Fierro, J. Structure and surface properties of ceria-modified Ni-based catalysts for hydrogen production. *Appl. Catal. B Environ.* **2018**, *225*, 340–353. [CrossRef]

32. Ho, P.; de Luna, G.S.; Angelucci, S.; Canciani, A.; Jones, W.; Decarolis, D.; Ospitali, F.; Aguado, E.; Rodríguez-Castellón, E.; Fornasari, G.; et al. Understanding structure-activity relationships in highly active La promoted Ni catalysts for CO_2 methanation. *Appl. Catal. B Environ.* **2020**, *278*, 119256. [CrossRef]

33. Mebrahtu, C.; Krebs, F.; Perathoner, S.; Abate, S.; Centi, G.; Palkovits, R. Hydrotalcite based $Ni–Fe/(Mg, Al)Ox$ catalysts for CO_2 methanation–tailoring Fe content for improved CO dissociation, basicity, and particle size. *Catal. Sci. Technol.* **2018**, *8*, 1016–1027. [CrossRef]

34. Ren, J.; Mebrahtu, C.; Palkovits, R. Ni-based catalysts supported on Mg–Al hydrotalcites with different morphologies for CO_2 methanation: Exploring the effect of metal–support interaction. *Catal. Sci. Technol.* **2020**, *10*, 1902–1913. [CrossRef]

35. Shen, L.; Xu, J.; Zhu, M.; Han, Y.-F. Essential Role of the Support for Nickel-Based CO_2 Methanation Catalysts. *ACS Catal.* **2020**, *10*, 14581–14591. [CrossRef]

36. Siakavelas, G.; Charisiou, N.; AlKhoori, S.; AlKhoori, A.; Sebastian, V.; Hinder, S.; Baker, M.; Yentekakis, I.; Polychronopoulou, K.; Goula, M. Highly selective and stable nickel catalysts supported on ceria promoted with Sm_2O_3, Pr_2O_3 and MgO for the CO_2 methanation reaction. *Appl. Catal. B Environ.* **2020**, *282*, 119562. [CrossRef]

37. Sterk, E.B.; Nieuwelink, A.-E.; Monai, M.; Louwen, J.N.; Vogt, E.T.C.; Filot, I.A.W.; Weckhuysen, B.M. Structure Sensitivity of CO_2 Conversion over Nickel Metal Nanoparticles Explained by Micro-Kinetics Simulations. *JACS Au* **2022**, *2*, 2714–2730. [CrossRef]

38. Ortega-Liebana, M.C.; Hueso, J.L.; Ferdousi, S.; Arenal, R.; Irusta, S.; Yeung, K.L.; Santamaria, J. Extraordinary sensitizing effect of co-doped carbon nanodots derived from mate herb: Application to enhanced photocatalytic degradation of chlorinated wastewater compounds under visible light. *Appl. Catal. B Environ.* **2017**, *218*, 68–79. [CrossRef]

39. Lin, L.; Gerlak, C.A.; Liu, C.; Llorca, J.; Yao, S.; Rui, N.; Zhang, F.; Liu, Z.; Zhang, S.; Deng, K.; et al. Effect of Ni particle size on the production of renewable methane from CO_2 over Ni/CeO_2 catalyst. *J. Energy Chem.* **2021**, *61*, 602–611. [CrossRef]

40. Marconi, E.; Tuti, S.; Luisetto, I. Structure-Sensitivity of CO_2 Methanation over Nanostructured Ni Supported on CeO_2 Nanorods. *Catalysts* **2019**, *9*, 375. [CrossRef]

41. Munnik, P.; Velthoen, M.E.Z.; de Jongh, P.E.; de Jong, K.P.; Gommes, C.J. Nanoparticle Growth in Supported Nickel Catalysts during Methanation Reaction-Larger is Better. *Angew. Chem.* **2014**, *126*, 9647–9651. [CrossRef]

42. Varvoutis, G.; Lykaki, M.; Stefa, S.; Binas, V.; Marnellos, G.E.; Konsolakis, M. Deciphering the role of Ni particle size and nickel-ceria interfacial perimeter in the low-temperature CO_2 methanation reaction over remarkably active Ni/CeO_2 nanorods. *Appl. Catal. B Environ.* **2021**, *297*, 120401. [CrossRef]

43. Vrijburg, W.L.; Moioli, E.; Chen, W.; Zhang, M.; Terlingen, B.J.; Zijlstra, B.; Filot, I.; Züttel, A.; Pidko, E.; Hensen, E.J. Efficient Base-Metal $NiMn/TiO_2$ Catalyst for CO_2 Methanation. *ACS Catal.* **2019**, *9*, 7823–7839. [CrossRef]

44. Wang, K.; Men, Y.; Liu, S.; Wang, J.; Li, Y.; Tang, Y.; Li, Z.; An, W.; Pan, X.; Li, L. Decoupling the size and support/metal loadings effect of Ni/SiO_2 catalysts for CO_2 methanation. *Fuel* **2021**, *304*, 121388. [CrossRef]

45. Shen, W.; Dumesic, J.; Hill, C. Criteria for stable Ni particle size under methanation reaction conditions: Nickel transport and particle size growth via nickel carbonyl. *J. Catal.* **1981**, *68*, 152–165. [CrossRef]

46. Santiago, M.; Groen, J.C.; Pérez-Ramírez, J. Carbon-templated hexaaluminates with enhanced surface area and catalytic performance. *J. Catal.* **2008**, *257*, 152–162. [CrossRef]

47. Barton, T.J.; Bull, L.M.; Klemperer, W.G.; Loy, D.A.; McEnaney, B.; Misono, M.; Monson, P.A.; Pez, G.; Scherer, G.W.; Vartuli, A.J.C.; et al. Tailored Porous Materials. *Chem. Mater.* **1999**, *11*, 2633–2656. [CrossRef]

48. Guo, J.; Lou, H.; Zhao, H.; Wang, X.; Zheng, X. Novel synthesis of high surface area $MgAl_2O_4$ spinel as catalyst support. *Mater. Lett.* **2004**, *58*, 1920–1923. [CrossRef]

49. Pereñiguez, R.; Gonzalez-Delacruz, V.M.; Caballero, A.; Holgado, J.P. $LaNiO_3$ as a precursor of Ni/La_2O_3 for CO_2 reforming of CH4: Effect of the presence of an amorphous NiO phase. *Appl. Catal. B Environ.* **2012**, *123–124*, 324–332. [CrossRef]

50. Pereñiguez, R.; Gonzalez-Delacruz, V.M.; Holgado, J.P.; Caballero, A. Synthesis and characterization of a $LaNiO_3$ perovskite as precursor for methane reforming reactions catalysts. *Appl. Catal. B Environ.* **2010**, *93*, 346–353. [CrossRef]

51. Ruckenstein, E.; Hu, Y. Interactions between Ni and La_2O_3 in Ni/La_2O_3 Catalysts Prepared Using Different Ni Precursors. *J. Catal.* **1996**, *161*, 55–61. [CrossRef]

52. Rodriguez-Gomez, A.; Caballero, A. Identification of Outer and Inner Nickel Particles in a Mesoporous Support: How the Channels Modify the Reducibility of Ni/SBA-15 Catalysts. *ChemNanoMat* **2016**, *3*, 94–97. [CrossRef]

53. Bueno-Alejo, C.J.; Arca-Ramos, A.; Hueso, J.L.; Santamaria, J. LED-driven continuous flow carbon dioxide hydrogenation on a nickel-based catalyst. *Catal. Today* **2020**, *355*, 678–684. [CrossRef]

54. Biesinger, M.C.; Payne, B.P.; Grosvenor, A.P.; Lau, L.W.M.; Gerson, A.R.; Smart, R.S.C. Resolving surface chemical states in XPS analysis of first row transition metals, oxides and hydroxides: Cr, Mn, Fe, Co and Ni. *Appl. Surf. Sci.* **2011**, *257*, 2717–2730. [CrossRef]

55. Biju, V.; Khadar, M.A. Electronic Structure of Nanostructured Nickel Oxide Using Ni2p XPS Analysis. *J. Nanoparticle Res.* **2002**, *4*, 247–253. [CrossRef]

56. McIntyre, N.S.; Johnston, D.D.; Coatsworth, L.L.; Davidson, R.D.; Brown, J.R. X-ray photoelectron spectroscopic studies of thin film oxides of cobalt and molybdenum. *Surf. Interface Anal.* **1990**, *15*, 265–272. [CrossRef]

57. Espinos, J.P.; Fernandez, A.R.; Gonzalezelipe, A.; Munuera, G. Electronic Interaction of Ni particles with TiO_2 and SiO_2. *Surf. Sci.* **1991**, *251*, 1012–1017. [CrossRef]

58. Czekaj, I.; Loviat, F.; Raimondi, F.; Wambach, J.; Biollaz, S.; Wokaun, A. Characterization of surface processes at the Ni-based catalyst during the methanation of biomass-derived synthesis gas: X-ray photoelectron spectroscopy (XPS). *Appl. Catal. A Gen.* **2007**, *329*, 68–78. [CrossRef]

59. Feng, C.; Zhang, Y.; Zhang, Y.; Wen, Y.; Zhao, J. Study on Alumina-Supported Cobalt–Nickel Oxide Catalyst for Synthesis of Acetonitrile from Ethanol. *Catal. Lett.* **2011**, *141*, 168–177. [CrossRef]

60. Guczi, L.; Stefler, G.; Geszti, O.; Sajó, I.; Pászti, Z.; Tompos, A.; Schay, Z. Methane dry reforming with CO_2: A study on surface carbon species. *Appl. Catal. A Gen.* **2010**, *375*, 236–246. [CrossRef]

61. Wiltner, A.; Linsmeier, C. Formation of endothermic carbides on iron and nickel. *Phys. Status Solidi A* **2004**, *201*, 881–887. [CrossRef]

62. Schmider, D.; Maier, L.; Deutschmann, O. Reaction Kinetics of CO and CO_2 Methanation over Nickel. *Ind. Eng. Chem. Res.* **2021**, *60*, 5792–5805. [CrossRef]

63. Cored, J.; García-Ortiz, A.; Iborra, S.; Climent, M.J.; Liu, L.; Chuang, C.-H.; Chan, T.-S.; Escudero, C.; Concepción, P.; Corma, A. Hydrothermal Synthesis of Ruthenium Nanoparticles with a Metallic Core and a Ruthenium Carbide Shell for Low-Temperature Activation of CO_2 to Methane. *J. Am. Chem. Soc.* **2019**, *141*, 19304–19311. [CrossRef]

64. Muroyama, H.; Tsuda, Y.; Asakoshi, T.; Masitah, H.; Okanishi, T.; Matsui, T.; Eguchi, K. Carbon dioxide methanation over Ni catalysts supported on various metal oxides. *J. Catal.* **2016**, *343*, 178–184. [CrossRef]

65. Rogers, J.L.; Mangarella, M.C.; D'Amico, A.D.; Gallagher, J.R.; Dutzer, M.R.; Stavitski, E.; Miller, J.T.; Sievers, C. Differences in the Nature of Active Sites for Methane Dry Reforming and Methane Steam Reforming over Nickel Aluminate Catalysts. *ACS Catal.* **2016**, *6*, 5873–5886. [CrossRef]

66. Malet, P.; Caballero, A. The selection of experimental conditions in temperature-programmed reduction experiments. *J. Chem. Soc. Faraday Trans. 1 Phys. Chem. Condens. Phases* **1988**, *84*, 2369–2375. [CrossRef]